Energy and the Environment

XANES-based determination of redox potentials imposed by steel corrosion products in cement-based media

Bin Ma, Alejandro Fernandez-Martinez, Benoît Madé, Nathaniel Findling, Ekaterina Markelova, Eduardo Salas-Colera, Thierry Maffeis, Aled Lewis, Delphine Tisserand, Sarah Bureau, and Laurent Charlet

Environ. Sci. Technol., **Just Accepted Manuscript** • DOI: 10.1021/acs.est.8b03236 • Publication Date (Web): 13 Sep 2018

XANES-based determination of redox potentials imposed by steel corrosion products in cement-based media

Bin Ma[*,a], Alejandro Fernandez-Martinez[*,a], Benoît Madé[b], Nathaniel Findling[a], Ekaterina Markelova[c], Eduardo Salas-Colera[d,e], Thierry G.G. Maffeis[f], Aled R. Lewis[f], Delphine Tisserand[a], Sarah Bureau[a], Laurent Charlet[a]

[a] Univ. Grenoble Alpes, Univ. Savoie Mont Blanc, CNRS, IRD, IFSTTAR, ISTerre, 38000 Grenoble, France.

[b] Andra, Research and Development Division, 1-7 rue Jean Monnet, Châtenay-Malabry 92298, France.

[c] Amphos21 Consulting S.L., Passeig de Garcia Fària, 49, 08019 Barcelona.

[d] Instituto de Ciencia de Materiales de Madrid, CSIC, Sor Juana Inés de la Cruz 3, 28049, Cantoblanco Madrid, Spain.

[e] Spanish CRG BM25 SpLine Beamline at the ESRF, 71 Avenue de Martyrs, F-38043 Grenoble, France.

[f] Systems and Process Engineering Centre, College of Engineering, Swansea University, Fabian Way, Swansea SA1 8EN, UK

ABSTRACT: The redox potential (Eh) in a cementitious nuclear waste repository is critical to the retardation behavior of redox-sensitive radionuclides (RNs), and largely controlled by embedded steel corrosion but hard to be determined experimentally. Here, we propose an innovative Eh determination method based on chemical/spectroscopic measurements. Oxidized nuclides (U^{VI}, Se^{IV}, Mo^{VI}, and Sb^{V}) were employed as species probes to detect the Eh values imposed by steel (Fe^0) and steel corrosion products (magnetite/hematite, and magnetite/goethite couples) in cement pore water. Nuclides showed good sorption affinity, especially towards Fe^0, in decreasing K_d order for U > Sb > Se > Mo under both N_2 and H_2 atmospheres. The reduced nuclide species were identified as UO_2, U_4O_9, FeSe, $FeSe_2$, Se^0, Sb^0, and Sb_2O_3, but no redox transformation occurred for Mo. Eh values were obtained by using the Nernst equation. Remarkably, their values fell in a small range centered around -456 mV at pH ~13.5 for both Fe^0 and Fe-oxyhydroxides couples. This Eh value appears to be controlled by the nano-crystalline $Fe(OH)_2/Fe(OH)_3$ or $(Fe_{1-x},Ca_x)(OH)_2/Fe(OH)_3$ couple, whose presence was confirmed by pair distribution function analyses. This approach could pave the way for describing the Eh gradient in reinforced concrete where traditional Eh measurements are not feasible.

1. INTRODUCTION

The redox potential (Eh) in a geological radioactive waste repository is of great importance to the migration behavior of redox-sensitive radionuclides (RNs) [1]. In France, a cementitious-rich repository in Callovo-Oxfordian clay system is foreseen [2, 3]. Reinforced concrete structures (e.g., alveoli and waste packages) are supposed to act as chemical barriers, limiting the mobility of RNs and isolating them from the biosphere. In such systems, the Eh is expected to be mainly controlled by the corrosion of embedded steel, producing a thin (over a few microns) dynamic Fe^{II}-oxyhydroxides/magnetite/Fe^{III}-oxyhydroxides "sandwich" film structure [4]. Less than five years after repository alveoli closure, the O_2 will be consumed, the system water saturated and the Eh will decrease, as imposed by the anoxic corrosion of steel and resulting hydrogen production [1]. A maximum H_2 pressure of 70 - 100 bars range [5] in the waste canister is expected and H_2 potentially acts as an electron donor for numerous oxidized nuclides species (e.g., U^{VI}, Se^{IV}, Mo^{VI}, and Sb^{V}) present at the site [6]. Due to the complex corrosion interfaces and unclear H_2(g) contribution, the actual Eh which will prevail in the alveoli still remains undetermined.

Steel corrosion products, from the inner to the outer level, can be white rust ($Fe(OH)_2$), magnetite (Fe_3O_4), goethite (α-FeOOH), and more condensed hematite (α-Fe_2O_3) [7]. Under aerobic conditions, Fe_3O_4 is the intermediate oxidation product on the steel surface while $Fe(OH)_2$ is the intermediate product under anaerobic conditions [8]. Previous studies have reported that the oxidized RN species can be immobilized by these Fe-oxyhydroxides via reductive precipitation and surface adsorption. Among the widely concerned RNs, U^{VI}, Se^{IV}, Sb^{V}, and Mo^{VI} are redox sensitive. U^{VI} can be reduced by ferrous iron on colloidal hematite [9], nanocrystalline magnetite [10, 11], and nanoscale zero-valent iron (NZVI) [12]. Besides, Fe^{III}-oxyhydroxides, e.g., goethite, can also remove aqueous U^{VI} by surface complexation [13]. Regarding aqueous Se^{IV}, reduced species, e.g., Se^0, FeSe, and $FeSe_2$, could be also obtained on these Fe-oxyhydroxides [14], concomitantly to surface adsorption processes. Fe-oxyhydroxides [15] and Fe^0 [16] also show strong sorption af-

finity to Sb^V, resulting in reductive precipitates (e.g., Sb_2O_3 and Sb^0) and structural incorporation [17, 18]. In contrast, molybdate is much more difficult to reduce, even by NZVI [19], and to adsorb on Fe-oxyhydroxides systems [20, 21]. After the oxidative alteration of spent nuclear fuel, the oxidized RN species should dominate [22, 23], having high solubility and thus low adsorption affinity to the iron products under alkaline conditions. Therefore, reductive immobilization can be considered as an important pathway to reduce their mobility. However, in hyperalkaline cement pore water (CPW), sorption behavior of these RN anions on Fe-oxyhydroxides is especially scarce and not well documented.

In the case of cementitious-rich repositories, both hyperalkaline and high H_2 partial pressure conditions would make it impossible to conduct regular Pt-electrode direct measurements of the interfacial Eh associated with the steel corrosion products. Large discrepancies exist between experimentally measured Eh and computed Nernstian values because the measurements are performed under conditions that are out of equilibrium [24] and the analytical difficulties associated with oxidation-reduction potential (ORP) electrodes [25, 26]. Recently, the redox potentials of structural Fe in clay minerals (i.e., smectites) were attempted to determine using organic one-electron-transfer mediating compounds under nearly neutral conditions [27-30]. However, under hyperalkaline conditions, i.e., in cementitious environment, the speciation and stability of organics may pose large uncertainties to the Eh determination. In this study, a combination of wet chemistry methods and synchrotron-based X-ray spectroscopic and scattering techniques, namely X-ray absorption near edge structure (XANES) and pair distribution function (PDF) analyses, was employed to describe RNs sorption behavior on NZVI and Fe-oxyhydroxides in CPW. The solid RN species are identified by the XANES analysis and the related thermodynamic data is gained from the literature. Here, the steel is modeled by NZVI [31]. Although steel and NZVI have big differences on ductility, hardness, and melting points, both their chemical properties should be controlled by ZVI. Compared to bulk ZVI, the high specific surface area of NZVI should result in more quickly reaching redox equilibrium and higher standard Gibbs

free energy of formation ($\Delta_f G^0$) (see Section 3.5). The aim of this study is to determine "in-situ" the experimental Eh imposed by the steel and its corrosion products couples, *e.g.*, magnetite/hematite (abbreviated as M/H) and magnetite/goethite (M/G), using redox-sensitive nuclides, *i.e.*, U, Se, Mo, and Sb, as the redox probes.

2. MATERIALS AND METHODS

2.1. Materials and Chemicals. Boiled and argon-degassed Milli-Q water (18.2 MΩ·cm) was used for all solutions and suspensions. Stable isotopes were always used as analogues of RNs. All chemicals used for synthesis and stock solutions, including Fe-salts (e.g., $FeCl_2{\cdot}4H_2O$, $FeCl_3{\cdot}6H_2O$, and $Fe(NO_3)_3{\cdot}9H_2O$) and chemicals for radionuclide anions (e.g., $Na_2SeO_3{\cdot}5H_2O$, $Na_2MoO_4{\cdot}2H_2O$, and $KSb(OH)_6$) , are analytical reagents. They were purchased from Sigma Aldrich and opened for the first time before use in the glove box. An acidic 1000 ppm UO_2Cl_2 stock solution was used as a U^{VI} source. Synthetic fresh CPW was prepared according to the recipe from CEA [32] and used as background solution in all reactors. Its pH value is ~13.5 and the composition is given in Table S1. All experiments were performed in a N_2-filled glove box (O_2<2 ppm, using NaOH as the CO_2 trap) to prevent oxidation and possible CO_2 contamination.

2.2. Synthesis and characterization of Fe-bearing phases.

NZVI, magnetite, hematite, and goethite were synthesized and washed according to the synthesis protocols (details shown in Text S1) as reported in previous works [33-37]. Except for NZVI, all the Fe-bearing phases were stored as suspensions at given solid to liquid (S/L) ratios in the glove box. After freeze-drying, the mineral purity of all Fe-bearing phases was checked by powder X-ray diffraction (XRD) analysis (CuK_α radiation), which indicated no distinct impurity diffraction peak (Figure S1). Mineral specific surface areas (Table S2) were measured by the Brunauer-Emmett-Teller (BET) N_2-absorption method, in order to verify the surface site concentration for sorption experiments. The size and shape of particles were further characterized by field emission scanning electron microscope (FE-SEM; Quanta FEG 250), shown in

Figure S2. The uniform nano-sized magnetite, hematite, and goethite, were present as spherical, rhombohedral, and needle shaped particles, respectively.

2.3. Batch sorption experiments. All sorption experiments were performed at a total surface-site concentration of 2×10^{-4} M, approximately. The site density is assumed to be at least 1 site nm^{-2} [38]. Thus, the corresponding requested S/L ratios in the reaction suspensions were found to be 4.17 g L^{-1} (NZVI), 1.60 g L^{-1} (magnetite) plus 2.86 g L^{-1} (hematite), and 1.60 g L^{-1} (magnetite) plus 6.12 g L^{-1} (goethite). To avoid co-precipitation of RN analogues and aqueous Ca^{2+} in CPW, RN analogue concentrations were set equal to 5×10^{-5} M for U and 2×10^{-4} M for the other three RN analogues (i.e., Se, Mo, and Sb). Thus, S/L ratios for U reactors were four times less than in other RN analogues reactors. Prior to introducing RN analogues, iron solid phases were equilibrated with CPW for 24 h, in order to reach steady (Figure S3). In addition, preliminary experiments were set to investigate the sorption kinetics of the four RN analogues (i.e., U, Se, Mo, and Sb) on NZVI and M/H in the glove box. Individual sorption experiments of the various RN analogues on each coupled steel products (i.e., NZVI, M/H, and M/G) were conducted at 25 °C under constant shaking in the glove box. After an equilibrium time of ~100 d, 4 mL of suspension were sampled from each reactor and filtered through 0.22-µm syringe filters. Parallel sorption experiments were conducted at 25 °C in H_2 atmosphere (P_{H2} = 8.0 bar) in stainless steel (T316) high pressure-high temperature reactors (PARR, USA)[39]. Two reaction times, 21 d and 70 d, were investigated to know the reaction process. After reaction, the solution pH was measured by a combined glass Micro-pH electrode (Metrohm 6.0234.100) immediately after its calibration. A combined Pt-ring ORP electrode (Metrohm 6.0451.100) was used for Eh measurement, after being calibrated with Zobell's solution (200 mV at 25 °C) [26]. Due to the extremely high pH conditions (pH ~ 13.5), it was difficult for the Eh probe to achieve a stable reading. Total aqueous Ca, S, Fe, U, Se, Mo, and Sb concentrations were analyzed by inductively coupled plasma optical emission spectrometry (ICP-OES) with a Varian 720-ES apparatus. The possible presence of aqueous reduced S (e.g., S^{2-}) and Sb (e.g., $Sb(OH)_4^-$) species

was checked using the methylene blue method[40] and high-performance liquid chromatography-mass spectrometry (HPLC-MS), respectively. The lower detection limits for S^{2-} and $Sb(OH)_4^-$ were 10 and 0.1 ppb, respectively. However, no reduced S and Sb species could be detected in solution (Figure S4). The distribution coefficient (K_d) was calculated according to a standard definition (Text S2).

Sorption products in each reactor were collected by vacuum filtration through 0.22-µm nitro-cellulose membrane, stored in glove box, and extreme care was taken to minimize the potential for sample oxidation during subsequent solid characterizations.

2.4. XANES spectroscopy. XANES spectroscopy measurements at selenium K-edge (12658 eV), uranium L_3-edge (17166 eV), molybdenum K-edge (20000 eV), and antimony K-edge (30491 eV), were conducted at the SpLine Spanish CRG Beamline (BM25A) at the European Synchrotron Radiation Facility (ESRF), Grenoble, France. For each element, energy calibration was done in parallel using the corresponding elemental foil, except for uranium. The U L_3-edge energy was calibrated by the K-edge excitation energy of an yttrium (17038 eV) metallic foil. The collected sorption products in batch sorption experiments were sealed double-side using Kapton tape in glove box, then transferred within an anaerobic chamber to the synchrotron facility. All samples were measured in fluorescence mode, except for the references which were prepared as pellets by diluting the solids in cellulose and measured in transmission mode. A Sirius liquid nitrogen cooled Si(Li) 13-multi-element solid state X-Ray detector from e2v was used for data collection. The obtained fluorescence signal was corrected for detector deadtime. During the measurement, samples were always under N_2 atmosphere protection. Each sample was scanned at least four times and the high consistency of the repeated scans indicated that no redox reaction occurred during the course of the measurements. The Demeter software package was used for data integration and reduction of XANES (Athena) [41]. A linear combination fit (LCF) was applied to the XANES spectra to identify and quantify the element species. The LCF was started with the best two reference spectra and the energy shift of references was fixed.

One more reference spectrum (n+1) would be added, only if a reduced χ square (χ_v^2) value of at least 15% lower than that of the best n-component fit was obtained (i.e., only if a significantly better fit was achieved) [42].

2.5. PDF analyses. Equilibrium products of NZVI with CPW at different contacting time were characterized by PDF method. The high-energy X-ray scattering experiments were performed in beamline ID31 at the ESRF, using energy of 78.3 keV and a Perkin Elmer XRD 1621 flat detector. To avoid any oxidation, the reacted NZVI fine powder was packed in Ø1 mm Kapton capillaries, and sealed in capillaries by epoxy glue inside the glove box. These loaded capillaries were stored in anaerobic conditions until put on the sample racks. NIST certified CeO_2 powder sample was used for instrumental calibration and empty capillary with the same specification for background subtraction. 2D images of the scattered intensity were collected with an acquisition time of 5 min per sample. The obtained images were integrated to one-dimensional diagrams using the Fit2D software [43]. PdfGetX3 code [44] was employed to perform background substraction, Compton and atomic scattering factor corrections, and to get the experimental PDFs. Calculated PDFs were obtained by PDFGui software [45]. After PDF data normalization by the incident photon flux, differential PDF (d-PDF) were obtained by subtracting the PDF pattern of pristine NZVI from those of NZVI samples contacted with CPW.

2.6. Thermodynamic modelling and Eh computation. The PHREEQC code [46], coupling with the THERMOCHIMIE database [47] and the latest OECD/NEA (2005) thermodynamic data for Se [48] and U [49], was employed to calculate the saturation index (SI) value of each potentially formed solid phase. In the PHREEQC input code, two ion pairs of Ca-SeO_3 (log*K*, 3.17) [50] and Ca-MoO_4 (log*K*, 3.09) [51], and two Sb solid phases of $NaSb(OH)_6$ (log*K*, -5.00) and $Ca[Sb(OH)_6]_2$ (log*K*, -12.55) [52], were added. The activity of each aqueous ion was calculated based on the Extended Debye-Huckel approach, whose parameters are provided in the thermodynamic database. PhreePlot program was used to plot the Eh-pH diagrams and the input parameters were described along with each diagram.

The Eh values of corresponding half-reactions could then be calculated according to the Nernst equation:

$$E_h = -\frac{\Delta_r G^0}{nF} - \frac{RT}{nF}\ln\frac{a_{Red}}{a_{Ox}} \quad (1)$$

Where *R* and *F* are the universal gas constant and Faraday constant, respectively, n is the moles number of electrons transferred, *a* is the chemical activity for the relevant species, and $\Delta_r G^0$ is the standard Gibbs free energy of reaction.

3. RESULTS AND DISCUSSION

3.1. Aqueous phase results.

Equilibrium kinetics of NZVI and M/H with CPW were conducted and results of chemical analyses are shown in Figure S3. The total aqueous S (prevalent as SO_4^{2-}) concentration in both reactors is almost constant, indicating that nearly no SO_4^{2-} can be adsorbed or reductively precipitated on NZVI or M/H. In contrast, most Ca^{2+} in CPW was removed within 2 h for M/H. The pH value (~13.5) of CPW is extremely high, above the points of zero charge of iron oxides, which are in the range of 6.3 (for magnetite) to 9.5 (for hematite and goethite) [37]. The resulting highly negative surface favors the cation adsorption. Ca^{2+} sorption on NZVI was relatively slow, and underwent two stages, with a first one lasting ~ 6 h and a second going until 24 h or even longer. Bare NZVI a has strong reducing ability towards water, due to its non-stabilized surface and high specific surface area [53]. The observed two stages of Ca^{2+} removal could be ascribed to surface adsorption followed by co-precipitation, or by diffusion into small pore spaces present in the altered layer of secondary iron products (e.g., Fe^{II}-hydroxide phases) that forms on the surface of the corroding NZVI.

Sorption kinetics of U, Se, and Sb on NZVI and M/H were studied, suggesting that the sorption process of U and Sb reached equilibrium after ~21 d on an end-over-end shaker in N_2 atmosphere (Figure S5). Se sorption on M/H probably did not reach a complete equilibrium after ~21 d, as a slight decrease of $[Se]_{aq}$ was still observed after ~15 d. More details were

discussed in Text S3. Aqueous results, including ion concentrations, pH, Eh (measured by ORP Pt-electrode), and K_d values, of batch sorption experiments are listed in Table S3-S5. Under N_2 atmosphere, Eh values for NZVI reactors changed with reaction time, from -740 mV at the beginning to -530 mV at equilibrium, approximately. The bottom Eh line of water stability domain, i.e. the H_2O/H_2 stability border calculated for P_{H2} = 1.0 bar at pH ~13.5, is -798.7 mV. Thus, the lowest Eh values reached in the NZVI reactors could be controlled by H_2O decomposition by NZVI (-849.7 mV for $Fe^0/Fe(OH)_2$). After reacting with H_2O, the NZVI surface became therefore covered by Fe^{II}-hydroxide reaction product and the imposed Eh values increased. In M/H and M/G reactors, the Eh values were close to about -440 mV. Regarding reactors in H_2 atmosphere (P_{H2} = 8.0 bar), the Eh values should be dictated by the dissolved H_2/H_2O couple equilibrium, resulting in a value of ~ -740 mV. Throughout sorption experiments, pH values in all the reactors were always constant and equal to ~13.5.

K_d values derived from reactions under both N_2 and H_2 atmosphere are shown in Figure 1a and 1b, respectively. The hydrogen atmosphere did not lead to any RN removal enhancement from the aqueous phase. The obtained K_d values indicate a decreasing affinity of Fe corrosion products for RNs in the order of U > Sb > Se > Mo. Aqueous U^{VI} concentration in equilibrium with hyperalkaline cement leachate, i.e., alkali/alkaline-earth uranates (e.g., $Na(UO_2)O(OH)\cdot(H_2O)_{0-1}$ and $CaUO_4$), can be present at very low concentration ($\sim 10^{-9}$ M) [54]. However, the filtrate of U^{VI}-CPW blank sample through 0.22-µm membrane filter can still have a $\sim 4\times10^{-5}$ M U^{VI} total "dissolved" concentration (Table S3), suggesting the possible presence of nano-sized uranate colloids dispersed in solution. If these U^{VI} nano-colloids were formed in the suspension, they would be stable for years [55]. However, they were likely to be removed rapidly from aqueous phase by the iron corrosion products. For antimony, the strong complexation affinity of Ca^{2+} for antimonite may also greatly contribute to the large K_d values observed for this element [52]. Among all the iron products, the NZVI phase led to the strongest sorption of all RNs. M/H couple showed a slightly larger sorption affinity to RNs than the

M/G couple. RN analogues sorption results in H_2 atmosphere with 21 d and 70 d reaction time, are shown in Table S4 and S5. After 21 d reaction, sorption of U and Sb reached equilibrium while the removal of Se and Mo still proceeded further.

3.2. Surface Se and Sb species.

Sorption products of batch experiments under N_2 and H_2 atmosphere were characterized by XANES. The references were measured, showing distinct RN species and different oxidation states. Linear combination fits (LCF) analysis of XANES was conducted to identify and quantify solid species of sorbed RN analogues (Figure 2). The LCF results for sorption products under N_2 conditions were listed in Table 1, while those for H_2 reactors in Table S6-S9. Experimental Se K-edge XANES spectra are shown in Figure 2a. In our system, sorbed selenium could be present as FeSe, $FeSe_2$, and Se^0 reduced species, or as Se^{IV} (surface) complexes and structurally incorporated Se^{IV} with Ca and Fe. The exact Se^{IV} solid species in such complicated systems are hard to describe by the common Se^{IV} references (e.g., Na_2SeO_3, $CaSeO_3$, and $FeSeO_3$) we measured. This could be responsible for the imperfect XANES spectrum reproduction by LCF. Nevertheless, the oxidation state of Se^{IV} can be identified exactly, which is the key point for the following Nernstian computation. In presence of NZVI, selenite can be reduced into FeSe and $FeSe_2$, while Fe-oxyhydroxides couples can only reduce selenite into Se^0. The reductant in the iron couples is magnetite, which can reduce selenite into Se^0 and even Fe selenides under slightly acid conditions [56, 57]. Previous report illustrate that selenite can be reduced into FeSe by Fe/FeC_3 ultrasmall particles at pH 4.8 – 8.0 and at pH 10.3 [58]. Here, in extremely alkaline solution (pH ~13.5), NZVI is also able to act as a powerful reductant towards selenite. According to LCF results of NZVI sample spectra, more FeSe was formed and the generated amount of reduced species was larger in presence of H_2, compared to the N_2 case. In presence of dissolved H_2, NZVI oxidation by water may be inhibited, and consequently other oxidation pathway, e.g., NZVI oxidation by selenite, could be favored. Besides, it can be clearly observed from XANES spectra that the formation of low oxidation

state Se species was proceeding within 70 days in H_2 reactors. In addition, adsorbed Se^{IV} was more likely to complex with Ca than to remain present as free ion.

For antimony, the introduced antimonate could be strongly associated with Ca^{2+} [52], i.e., as a $Ca[Sb(OH)_6]_2^0$ soluble complex and $Ca[Sb(OH)_6]_2(s)$ precipitates, while forming with Fe^{III} hydroxides octahedral inner-sphere surface complexes [18]. In reducing environment, lower oxidation state Sb species, e.g., Sb^{III} and Sb^0, can be formed. For instance, magnetite can reduce Sb^V into Sb^{III} and the reduction increases with increasing pH values [15]. Sb^{III} was also found present at the surface of Fe-bearing rims [59]. In addition, Sb^0 was detected in soil samples from Swiss shooting ranges, probably derived from reduction by Pb^0 present in PbSb alloy-containing unweathered bullet fragments [18]. Thus, Fe^0, with lower standard reduction potential than Pb^0, can also generate Sb^0 [16]. Experimental Sb K-edge XANES spectra are shown in Figure 2b. Sb_2O_3 was detected prevalently in all sorption products, while Sb^0 was identified only in the NZVI reactors. Although all H_2 reactors had very low redox potentials (Table S4 and S5), closed to values recorded in NZVI reactors, no Sb^0 was observed in Fe oxide-couples reactors. The redox potentials imposed by Fe-oxide couples are not low enough to generate the most reduced Sb species, Sb^0. Thus, the absence of Sb^0 as a product in Fe oxide-couple reactors, even in the presence of $H_2(g)$, was probably due to a lack of sufficient $H_2(g)$ adsorption/reaction interfaces, or a lack of catalytic mediums (e.g., precious metals), or not high enough reaction temperature (i.e., room temperature) and $H_2(g)$ partial pressure (i.e., P_{H2} = 8.0 bar). From the LCF results for NZVI reactors, introducing H_2 resulted in larger molar fractions of formed Sb^0. The XANES reference sample of Sb^V sorbed on goethite was prepared by mixing $K[Sb(OH)_6]$ stock solution with Fe oxyhydroxides in CPW. As shown in Table 1 and S7, Sb^V-goethite surface complex and $Ca[Sb(OH)_6]_2(s)$ precipitate contribute largely to the total sorbed Sb^V species signal observed on Fe-oxyhydroxides couples, which the originally introduced $K[Sb(OH)_6]$ contribution is small.

3.3. Surface U and Mo species.

As demonstrated by Bots et al [55], uranium total trace aqueous concentration in equilibrium with CPW should be extremely low (~10^{-9} M), as U^{VI} prefers to form mobile metal (e.g., Ca, Na, and K) uranate(VI) nano-colloids. The XANES reference of uranate(VI) was prepared by mixing Ca^{2+}, Na^{+}, and UO_2^{2+} at pH ~13. Experimental U L3-edge XANES spectra were shown in Figure 2c. Fitting the spectra with a large number of references ($UO_3 \cdot 2H_2O$, uranate(VI), $UO_2(NO_3)_2 \cdot 6H_2O$[60], $NaUO_3$, U_4O_9, U_3O_8 [61], and UO_2 [62]), three potential components, i.e., uranate(VI), U_4O_9 and UO_2, of U sorption products were identified. LCF results showed that all adsorbed U^{VI} was uranate(VI), in accordance with results from Bots et al [55]. Once uranyl was introduced into the CPW suspension of iron particles, uranyl ion would complex with alkali or alkali-earth cations and transform into metal uranates(VI) colloids or complexes, immediately, which could thereafter aggregate or be sorbed on iron surface to allow further redox reactions to occur. Regarding potential reduction reactions, only NZVI was able to reduce U^{VI} into pure U^{IV}, and more UO_2 was generated in H_2 reactors than in the N_2 reactors. Instead, U reduced species in reactors of Fe-oxyhydroxides couples were always present as U_4O_9, a +4 and +6 mixed valence solid compound. Previous work also indicated that UO_2 should be the reduction product of U^{VI} on the surface of magnetite and the reaction to be facilitated by electron transfer between the Fe and U [11]. Indeed, regarding the U L3-edge XANES spectra of UO_2 and U_4O_9, their similar shapes and close white-line positions (~ 1 eV difference) increase the difficulty to distinguish the two species very clearly [60], thus lower the LCF accuracy (uncertainties were shown in Table 1 and S8). However, it is certain that reduced U species with oxidation states between +4 and +4.5 were present.

Regarding molybdenum, the XANES spectra are shown in Figure 2d. For Mo sorbed on NZVI, no reduction can be observed from XANES spectra. However, removal of aqueous Mo by NZVI is not negligible compared to removal by the Fe-oxyhydroxides couples. As shown in Figure 2d, Mo^{VI} pre-edge peak intensity of sorption products is quite weak, and similar to $FeMoO_4$ pre-edge peak. Thus, based on LCF analysis, a considerable amount of $FeMoO_4$ existed in the

sorption products. The decreased pre-edge intensity suggests that the tetrahedral MoO_4^{2-} was distorted and octahedral Mo [63] may probably form inner-sphere structural coordination with iron during the Fe^0 oxidation and further $Fe(OH)_2$ formation.

3.4. PDF analysis of reacted NZVI. Once suspended in CPW, the negatively surface charge of NZVI passivation coatings could lead to a large Ca^{2+} adsorption (Section 3.1) and meanwhile NZVI could still react with water molecules. It is then intriguing to understand the possible role of Ca in the promotion of "in-situ" NZVI corrosion process. NZVI samples, suspended in CPW for different times, were characterized by PDF analysis. The d-PDF patterns obtained after subtracting the PDF of pristine NZVI from NZVI reacted with CPW for 10 min, 23 h, 72 h, 168 h, and 264 h, are shown in Figure 3a. By subtracting the NZVI signal, several negative differential reflections can be observed, in accordance with Fe-Fe reflections of pristine NZVI (e.g., at 2.52 Å, 4.10 Å, 4.84 Å, and 6.38 Å), meaning that part of the NZVI was transformed into another phase. Positive differential reflections, at 2.13 Å, 3.33 Å, and 3.63 Å, were also observed. Compared to reference patterns of $Fe(OH)_{2(cr)}$ and $Ca(OH)_2$, these three reflections can be attributed to Fe-O, Fe-Fe, and Ca-Ca scattering pairs, respectively. The continuously increased positive differential signals of Fe-O and Fe-Fe indicate that NZVI was oxidized by water into $Fe(OH)_2$ gradually. In addition, the positive Ca-Ca signal can be derived from Ca^{2+} surface adsorption and possible $Ca(OH)_2$ solid phase formation. The $d_{Fe\text{-}O}$ at 2.13 Å was easily identified as it is nearly the distance observed within $Fe(OH)_{2(cr)}$ reference compound. In contrast, 3.33 Å and 3.63 Å distances in d-PDF were correspondingly ~0.07 Å longer than Fe-Fe distance (3.26 Å) in $Fe(OH)_{2(cr)}$ and Ca-Ca distance (3.57 Å) in $Ca(OH)_2$. These discrepancies may be due i) to limited instrumental resolution or, more likely, ii) to the fact that Fe^{II} and Ca^{II} hydroxides formed exhibited significant structural disorder. Note that Ca-Ca reflection at 3.63 Å continued to increase after 72 h and clearly separated from Fe-Fe at 3.33 Å. Later on, the intensity of the Ca-Ca peak decreased steeply and tended to merge with the Fe-Fe peak into a broaden peak

after 264 h. Meanwhile, aqueous Ca^{2+} concentration curves indicated no Ca^{2+} desorption according to sorption kinetic experiments. Thus, two reaction processes are occurring concomitantly at the NZVI particle surface: i) Ca^{2+} adsorption and $Ca(OH)_2$ precipitation, ii) Fe^0 oxidation into $Fe(OH)_2$. The first process is faster (see Section 3.1), forming an amorphous $Ca(OH)_2$ surface precipitate. The pH value (~13.5) imposed by hyperalkaline CPW is higher than the onset of precipitation of both Ca and Fe, which should provide favorable conditions to co-precipitation of Ca^{2+}, $Fe^{2+,}$ and OH^-. Thus, small amounts of a $(Fe_{1-x},Ca_x)(OH)_2$ solid solution might have formed. The surface of reacted NZVI at 264 h reaction time was also studied by X-ray photoelectron spectroscopy (XPS) analysis (Figure S6). An analysis of the Fe $2p_{3/2}$ region yielded three contributions of Fe^0 metal, Fe(II)-O, and Fe(III)-O, of which the Fe(III)-O contribution may result from oxygen oxidation during sample preparation and transfer to the XPS facility. Besides, the strong Ca(II)-O peak in the Ca 2p region indicated that Ca^{II} formed separate $Ca(OH)_2$ solid phase or it was incorporated into the surface of reacted NZVI during the formation of Fe^{II} hydroxides. In addition, a previous report also showed that a rather thick (50 - 200 μm) and porous layer of iron oxides interspersed with $Ca(OH)_2$ forms with time [64]. The adsorbed/co-precipitated $(Fe_{1-x},Ca_x)(OH)_2$ may act as a corrosion passivation layer, increasing Fe^{II} hydroxide solubility and further shifting the interfacial Eh values to lower values.

Within 45 days reaction time, NZVI totally transformed into $Fe(OH)_2$, as shown in Figure 3b. The broad diffraction peaks indicate the formation of nanocrystalline precipitates, compared to crystalline $Fe(OH)_2$ (Figure 3b). A 0.2 mM SeO_3^{2-} solution was added to react with $Fe(OH)_2$ on the surface. Although Se^{IV} can thermodynamically oxidize $Fe(OH)_2$ into Fe^{III}-hydroxides, no new Fe^{III} phase, like goethite or magnetite, could be observed in PDF data probably due to the low Se loading.

3.5. "In-situ" experimental Eh values. As shown from the above kinetic experiments, we assumed these species to be at chemical equilibrium. Eh-pH diagrams can then be drawn using

PhreePlot code [65] and Andra Thermochimie database [47], under conditions prevailing in our experiments (Figure S7). For each RN, various solid reduced species were considered and allowed to precipitate according to thermodynamics. Regarding aqueous RN analogue species, MoO_4^{2-} predominates for Mo and $UO_2(OH)_4^{2-}$ for U. For Se and Sb, besides SeO_3^{2-} and $Sb(OH)_6^-$ which predominate in oxic environments, HSe^- and $Sb(OH)_4^-$ aqueous species may also exist at equilibrium in reducing environments, especially HSe^- in Fe-poor reducing cement system [66]. However, as they are controlled by the precipitation of very insoluble FeSe and valentinite, HSe^- and $Sb(OH)_4^-$ aqueous concentrations can be assumed to be extremely low. Indeed, no HPLC retention peak was observed for $Sb(OH)_4^-$. Thus, the total aqueous concentration can be in all cases considered equal to the concentration of the dominant oxidized species. The LCF analysis identified reduced species for each RN analogue and quantified their fractional ratio within the solid phases. After, a set of redox reactions susceptible to occur between RN analogue couples and the considered iron product couples are identified and listed in Table 2.

All the $\Delta_f G^0$ of RN analogue species were taken from Andra ThermoChimie database [47], and are listed in Table S10. The activities of solid phases and water were set equal to 1.0 as first approximation, although this may not fully be true due, *e.g.*, to the nanosize of reductively precipitated solid phases. Besides, surface adsorption of anions can be negligible at pH ~13.5 and we assumed the activity of any potential adsorbed RN species to be equal to 1.0. "In-situ" experimental Eh values were then calculated according to equation (1) and are found to fall within the stability domain of water, whose lower limit is -798.7 mV at pH 13.5 (Figure 4). The $Fe(0)/Fe(OH)_2$ couple should impose an Eh value of -849.7 mV, outside the stability domain of water, and this may account for the observed formation of Sb^0 according to the Sb(III)/Sb(0) limit depicted in Figure S8. For all other RN analogue species, experimental Eh values of all NZVI systems are all centered in the narrow range of -441.3±65.6 mV (Figure 4). For reactors with the M/H redox couple, the obtained Eh values lay between ~-355.6 mV and ~-514.0 mV, with an average value of ~-468 mV and a large standard deviation. The Eh

values obtained in M/G reactors were slightly higher, probably due to a higher Eh (average value is -575.6 mV) imposed by M/G, compared to M/H couple (-649.0 mV).

Using the $\Delta_f G^0$ values listed in Table S10, the Eh values imposed by the various couples were computed, to compare with the experimental Eh values derived from individual RN half-cell redox reactions. In the case of NZVI, at least two Fe-oxyhydroxides couples, i.e., two interfacial Eh values, should be considered due to the fast oxidation of NZVI by water: the $Fe(0)/Fe(OH)_2$ couple and $Fe(OH)_2/Fe(OH)_3$ couple. $\Delta_f G^0$ values are critical to Eh calculation. According to PDF results, an amorphous $Fe(OH)_2$ phase or a Fe-Ca solid solution, such as $(Fe_{1-x},Ca_x)(OH)_2$, are present and will be characterized by larger solubility product (K_{sp}), and thus larger $\Delta_f G^0$ than corresponding crystalline phases. Using $\Delta_f G^0$ values of amorphous $Fe(OH)_2$ [37] and $Fe(OH)_3$ [67], the theoretical Eh imposed by $Fe(OH)_2/Fe(OH)_3$ couple was calculated to be equal to -456.4 mV, a value very closed to the experimental Eh values computed for the NZVI reactors. Theoretical Eh values from M/H (-649.0 mV) and M/G (-575.6 mV) couples were significantly lower than the experimental single RN half-reaction Eh values. Note that the two computed Eh values were derived from bulk Fe-oxyhydroxides and do not take into account surface energy [68] and surface hydration contributions [38] caused by nano-sized reaction particles, which would tend to increase $\Delta_f G^0$. The $\Delta_f G^0$ (+) correction factors (Table S11) were calculated using the method described by Silvester et al [38]. After applying the surface energy adjustments, the theoretical Eh values of M/H and M/G couples became -675.1 mV and -523.5 mV, respectively. As all the three Fe-oxyhydroxides are nano-sized, the adjustments in one couple can be counteracted. Thus, the effect of nano sizes cannot explain the Eh disagreements observed for the Fe couples. However, another acceptable way to explain experimental Eh distribution in M/H and M/G reactors can be a control by formed amorphous $Fe(OH)_2/Fe(OH)_3$ couple on the surface. In extremely alkaline CPW, most dissolved Fe^{2+} and Fe^{3+} present on the surface of Fe-oxyhydroxides could precipitate instantaneously

into amorphous $Fe(OH)_2$ and $Fe(OH)_3$ phases, and then participate in the following redox reactions, listed in Table 2.

3.6. Environmental Implications.

Concrete is the most used manufactured material worldwide. Within reinforced concrete, iron corrosion interfaces control to a large extent the durability of the material. These complex interfaces result in strong Eh gradient from the steel surface outwards to the concrete bulk. When the concrete is used in anoxic systems (polluted harbors, under seawater tunnels, bridges fundaments in bay sediments, nuclear repositories), the competition between redox conditions imposed from the outside (bedrock, sediment) and from inside (steel corrosion) will dictate the redox conditions prevailing within the concrete. In our CPW-systems, all the experimental redox potentials obtained from RNs half-reactions and redox coupled species concentration measurements pointed out to a unique central value of ~ -456 mV. This value is probably imposed by the amorphous $Fe(OH)_2/Fe(OH)_3$ or $(Fe_{1-x},Ca_x)(OH)_2/Fe(OH)_3$ couple, rather than by the originally added Fe-oxyhydroxides.

Disagreements between computed Nernstian Eh and electrode-measured Eh values are frequently reported in the literature [24]. The severe hyperalkaline cement environment prevailing e.g. in geological repositories, where $H_2(g)$ is also expected to occur, prevents experimental Eh determination using Pt-electrodes. In contrast, the approach described here shows a good internal consistency among all individual RN half-reaction Eh values and thus appear to be a reliable new method to compute Eh in concrete, but also in other (e.g., biological) systems where local Eh direct measurement is not feasible. This combination of spectroscopic techniques and wet chemistry methods allows thus an *ab initio* reliable Eh experimental determination through the use of the Nernst equation. Determination of redox potential is crucial for

the assessment of the long-term safety conditions of nuclear repositories. This study will facilitate the estimation of the "experimental" redox potential in reinforced cement matrix, allowing a better evaluation of RNs redox behavior and mobility.

ASSOCIATED CONTENT

Supporting Information Available. Additional materials referenced in the text are available free of charge.

XRD patterns, FE-SEM micrographs, and specific surface area of synthesized NZVI and Fe-oxyhydroxides. Fe-oxyhydroxides equilibrium and RN analogue sorption kinetics. HPLC analysis of aqueous Sb. XPS spectra of equilibrated NZVI. Eh-pH diagrams of RNs systems. Eh values out of water stability domain. CPW content. Aqueous results of reactors in N_2 and H_2 atmosphere. LCF results of XANES. List of $\Delta_f G^0$ values used. Surface energy contributions to $\Delta_f G^0$ values.

AUTHOR INFORMATION

Corresponding Authors

*Phone: +33(0) 7 67 13 83 83. E-mail: mabinpku@gmail.com (B. MA).

Phone: +33(0) 4 76 63 51 97. E-mail: Alex.Fernandez-Martinez@univ-grenoble-alpes.fr (A. FERNANDEZ-MARTINEZ).

Notes

The authors declare no competing financial interest.

ACKNOWLEDGMENTS

Dr. Fabrizio Bardelli is thanked for his helpful suggestions on XANES data interpretations. This work has been supported by a grant from the French National Radioactive Waste Management Agency (Andra), with partial funding from Labex OSUG@2020 [investissements

d'avenir; ANR10 LABX56]. B.M. also thanks the financial support from the China Scholarship Council (CSC). The synchrotron facilities ESRF (BM25A-25-01-976 and ID31) are acknowledged for the allocation of beamtime.

REFERENCES

(1) Duro, L.; Domènech, C.; Grivé, M.; Roman-Ross, G.; Bruno, J.; Källström, K. Assessment of the evolution of the redox conditions in a low and intermediate level nuclear waste repository (SFR1, Sweden). *Appl. Geochem.* **2014,** *49*, 192-205.

(2) Grambow, B. Mobile fission and activation products in nuclear waste disposal. *J. Contam. Hydrol.* **2008,** *102* (3-4), 180-186.

(3) Landais, P. Advances in geochemical research for the underground disposal of high-level, long-lived radioactive waste in a clay formation. *J. Geochem. Explor.* **2006,** *88* (1), 32-36.

(4) Nóvoa, X. R. Electrochemical aspects of the steel-concrete system. A review. *J. Solid State Electrochem.* **2016,** *20* (8), 2113-2125.

(5) Truche, L.; Berger, G.; Destrigneville, C.; Pages, A.; Guillaume, D.; Giffaut, E.; Jacquot, E. Experimental reduction of aqueous sulphate by hydrogen under hydrothermal conditions: Implication for the nuclear waste storage. *Geochim. Cosmochim. Acta* **2009,** *73* (16), 4824-4835.

(6) Truche, L.; Berger, G.; Destrigneville, C.; Guillaume, D.; Giffaut, E. Kinetics of pyrite to pyrrhotite reduction by hydrogen in calcite buffered solutions between 90 and 180 °C: Implications for nuclear waste disposal. *Geochim. Cosmochim. Acta* **2010,** *74* (10), 2894-2914.

(7) Antunes, R. A.; Costa, I.; Faria, D. L. A. d. Characterization of corrosion products formed on steels in the first months of atmospheric exposure. *Mater. Res.* **2003,** *6*, 403-408.

(8) Gouda, V. K. Corrosion and corrosion inhibition of reinforcing steel: I. Immersed in alkaline solutions. *Br. Corros. J.* **1970,** *5* (5), 198-203.

(9) Liger, E.; Charlet, L.; Van Cappellen, P. Surface catalysis of uranium (VI) reduction by iron (II). *Geochim. Cosmochim. Acta* **1999,** *63* (19), 2939-2955.

(10) Missana, T.; Maffiotte, U.; Garcia-Gutierrez, M. Surface reactions kinetics between nanocrystalline magnetite and uranyl. *J. Colloid Interface Sci.* **2003,** *261* (1), 154-160.

(11) Scott, T. B.; Allen, G. C.; Heard, P. J.; Randell, M. G. Reduction of U(VI) to U(IV) on the surface of magnetite. *Geochim. Cosmochim. Acta* **2005,** *69* (24), 5639-5646.

(12) Yan, S.; Hua, B.; Bao, Z.; Yang, J.; Liu, C.; Deng, B. Uranium(VI) removal by nanoscale zerovalent iron in anoxic batch systems. *Environ. Sci. Technol.* **2010,** *44* (20), 7783-7789.

(13) Sherman, D. M.; Peacock, C. L.; Hubbard, C. G. Surface complexation of U(VI) on goethite (α-FeOOH). *Geochim. Cosmochim. Acta* **2008,** *72* (2), 298-310.

(14) Fernandez-Martinez, A.; Charlet, L. Selenium environmental cycling and bioavailability: a structural chemist point of view. *Rev. Environ. Sci. Bio-Technol.* **2009**, *8* (1), 81-110.

(15) Kirsch, R.; Scheinost, A. C.; Rossberg, A.; Banerjee, D.; Charlet, L. Reduction of antimony by nano-particulate magnetite and mackinawite. *Mineral. Mag.* **2008,** *72* (1), 185-189.

(16) Zhou, Z.; Dai, C.; Zhou, X.; Zhao, J.; Zhang, Y. The removal of antimony by novel NZVI-zeolite: the role of iron transformation. *Water Air Soil Pollut.* **2015,** *226* (3), 76.

(17) Mitsunobu, S.; Muramatsu, C.; Watanabe, K.; Sakata, M. Behavior of antimony(V) during the transformation of ferrihydrite and its environmental implications. *Environ. Sci. Technol.* **2013,** *47* (17), 9660-9667.

(18) Scheinost, A. C.; Rossberg, A.; Vantelon, D.; Xifra, I.; Kretzschmar, R.; Leuz, A.-K.; Funke, H.; Johnson, C. A. Quantitative antimony speciation in shooting-range soils by EXAFS spectroscopy. *Geochim. Cosmochim. Acta* **2006,** *70* (13), 3299-3312.

(19) Huang, Y. H.; Tang, C.; Zeng, H. Removing molybdate from water using a hybridized zero-valent iron/magnetite/Fe(II) treatment system. *Chem. Eng. J.* **2012,** *200-202*, 257-263.

(20) Xu, N.; Christodoulatos, C.; Braida, W. Modeling the competitive effect of phosphate, sulfate, silicate, and tungstate anions on the adsorption of molybdate onto goethite. *Chemosphere* **2006,** *64* (8), 1325-1333.

(21) Das, S.; Jim Hendry, M. Adsorption of molybdate by synthetic hematite under alkaline conditions: Effects of aging. *Appl. Geochem.* **2013,** *28*, 194-201.

(22) Chen, F. R.; Burns, P. C.; Ewing, R. C. Near-field behavior of Tc-99 during the oxidative alteration of spent nuclear fuel. *J. Nucl. Mater.* **2000,** *278* (2-3), 225-232.

(23) Chen, F. R.; Burns, P. C.; Ewing, R. C. Se-79: Geochemical and crystallo-chemical retardation mechanisms. *J. Nucl. Mater.* **1999,** *275* (1), 81-94.

(24) Lindberg, R. D.; Runnells, D. D. Ground water redox reactions: An analysis of equilibrium state applied to Eh measurements and geochemical modeling. *Science* **1984,** *225* (4665), 925-927.

(25) Stumm, W.; Morgan, J. J. *Aquatic Chemistry: Chemical Equilibria and Rates in Natural Waters,*3rd ed.; John Wiley & Sons: New York, 1995; Vol. *126*.

(26) Markelova, E.; Parsons, C. T.; Couture, R.-M.; Smeaton, C. M.; Madé, B.; Charlet, L.; Van Cappellen, P. Deconstructing the redox cascade: what role do microbial exudates (flavins) play? *Environ. Chem.* **2017,** *14* (8), 515-524.

(27) Hofstetter, T. B.; Neumann, A.; Schwarzenbach, R. P. Reduction of nitroaromatic compounds by Fe(II) species associated with iron-rich smectites. *Environ. Sci. Technol.* **2006,** *40* (1), 235-242.

(28) Gorski, C. A.; Aeschbacher, M.; Soltermann, D.; Voegelin, A.; Baeyens, B.; Marques Fernandes, M.; Hofstetter, T. B.; Sander, M. Redox properties of structural Fe in clay minerals. 1. Electrochemical quantification of electron-donating and-accepting capacities of smectites. *Environ. Sci. Technol.* **2012,** *46* (17), 9360-9368.

(29) Gorski, C. A.; Klüpfel, L.; Voegelin, A.; Sander, M.; Hofstetter, T. B. Redox properties of structural Fe in clay minerals. 2. Electrochemical and spectroscopic characterization of

549 electron transfer irreversibility in ferruginous smectite, SWa-1. *Environ. Sci. Technol.* **2012,**
550 *46* (17), 9369-9377.
551 (30) Gorski, C. A.; Klüpfel, L. E.; Voegelin, A.; Sander, M.; Hofstetter, T. B. Redox
552 properties of structural Fe in clay minerals: 3. Relationships between smectite redox and
553 structural properties. *Environ. Sci. Technol.* **2013,** *47* (23), 13477-13485.
554 (31) Santos-Juanes, L.; García Einschlag, F. S.; Amat, A. M.; Arques, A. Combining ZVI
555 reduction with photo-Fenton process for the removal of persistent pollutants. *Chem. Eng. J.*
556 **2017**, *310*, 484-490.
557 (32) Macé, N.; Nerfie, P.; Coreau, N.; Thory, E.; Le Bescop, P.; Touze, G. *Préparation et*
558 *caractérisations des PCH CEM V/A ROMBAS dans le cadre du GL CTEC.* Report CEA,
559 DPC/SECR/ST/2015/057 indice A, 2015.
560 (33) Kanel, S. R.; Manning, B.; Charlet, L.; Choi, H. Removal of arsenic(III) from
561 groundwater by nanoscale zero-valent iron. *Environ. Sci. Technol.* **2005,** *39* (5), 1291-1298.
562 (34) Dixit, S.; Hering, J. G. Comparison of arsenic(V) and arsenic(III) sorption onto iron
563 oxide minerals: Implications for arsenic mobility. *Environ. Sci. Technol.* **2003,** *37* (18), 4182-
564 4189.
565 (35) Matijević, E.; Scheiner, P. Ferric hydrous oxide sols: III. Preparation of uniform particles
566 by hydrolysis of Fe (III)-chloride, -nitrate, and -perchlorate solutions. *J. Colloid Interface Sci.*
567 **1978,** *63* (3), 509-524.
568 (36) Penners, N.; Koopal, L. Preparation and optical properties of homodisperse haematite
569 hydrosols. *Colloids Surf.* **1986,** *19*, (2), 337-349.
570 (37) Cornell, R. M.; Schwertmann, U. *The Iron Oxides: Structure, Properties, Reactions,*
571 *Occurrences and Uses*, 2nd ed.; Wiley-VCH Verlag GmbH & Co. KGaA: Weinheim,
572 Germany, 2003.

(38) Silvester, E.; Charlet, L.; Tournassat, C.; Gehin, A.; Grenèche, J.-M.; Liger, E. Redox potential measurements and Mössbauer spectrometry of Fe^{II} adsorbed onto Fe^{III} (oxyhydr)oxides. *Geochim. Cosmochim. Acta* **2005,** *69* (20), 4801-4815.

(39) Didier, M.; Leone, L.; Greneche, J.-M.; Giffaut, E.; Charlet, L. Adsorption of hydrogen gas and redox processes in clays. *Environ. Sci. Technol.* **2012,** *46* (6), 3574-3579.

(40) Wan, M.; Shchukarev, A.; Lohmayer, R.; Planer-Friedrich, B.; Peiffer, S. Occurrence of surface polysulfides during the interaction between ferric (hydr)oxides and aqueous sulfide. *Environ. Sci. Technol.* **2014,** *48* (9), 5076-5084.

(41) Ravel, B.; Newville, M., ATHENA, ARTEMIS, HEPHAESTUS: data analysis for X-ray absorption spectroscopy using IFEFFIT. *J. Synchrotron Radiat.* **2005,** *12* (4), 537-541.

(42) Rimondi, V.; Bardelli, F.; Benvenuti, M.; Costagliola, P.; Gray, J. E.; Lattanzi, P. Mercury speciation in the Mt. Amiata mining district (Italy): Interplay between urban activities and mercury contamination. *Chem. Geol.* **2014,** *380*, 110-118.

(43) Hammersley, A. P.; Svensson, S. O.; Hanfland, M.; Fitch, A. N.; Hausermann, D. Two-dimensional detector software: From real detector to idealised image or two-theta scan. *High Pressure Res.* **1996,** *14* (4-6), 235-248.

(44) Juhas, P.; Davis, T.; Farrow, C. L.; Billinge, S. J. L. PDFgetX3: a rapid and highly automatable program for processing powder diffraction data into total scattering pair distribution functions. *J. Appl. Crystallogr.* **2013,** *46* (2), 560-566.

(45) Farrow, C.; Juhas, P.; Liu, J.; Bryndin, D.; Božin, E.; Bloch, J.; Proffen, T.; Billinge, S. PDFfit2 and PDFgui: computer programs for studying nanostructure in crystals. *J. Phys.: Condens. Matter* **2007,** *19* (33), 335219.

(46) Parkhurst, D. L.; Appelo, C. *User's guide to PHREEQC (version 2): A computer program for speciation, batch-reaction, one-dimensional transport, and inverse geochemical calculations;* **1999**.

598 (47) Giffaut, E.; Grivé, M.; Blanc, P.; Vieillard, P.; Colàs, E.; Gailhanou, H.; Gaboreau, S.;
599 Marty, N.; Made, B.; Duro, L. Andra thermodynamic database for performance assessment:
600 ThermoChimie. *Appl. Geochem.* **2014,** *49*, 225-236.
601 (48) Olin;, Å.; Nolang, B.; Osadchii, E. G.; Öhman, L.-O.; Rosen, E. *Chemical*
602 *Thermodynamics 7: Chemical Thermodynamics of Selenium*; OECD Nuclear
603 Agency/Elsevier: Amsterdam, 2005.
604 (49) Hummel, W.; Mompean, F. J.; Illemassène, M.; Perrone, J. *Chemical thermodynamics of*
605 *compounds and complexes of U, Np, Pu, Am, Tc, Se, Ni and Zr with selected organic ligands*;
606 Elsevier Science, 2005; Vol. *9*.
607 (50) Séby, F.; Potin-Gautier, M.; Giffaut, E.; Borge, G.; Donard, O. F. X. A critical review of
608 thermodynamic data for selenium species at 25°C. *Chem. Geol.* **2001**, *171* (3-4), 173-194.
609 (51) Essington, M. E. Calcium molybdate solubility in spent oil shale and a preliminary
610 evaluation of the association constants for the formation of $CaMoO_4^0$(aq), $KMoO_4^-$(aq), and
611 $NaMoO_4^-$(aq). *Environ. Sci. Technol.* **1990,** *24* (2), 214-220.
612 (52) Johnson, C. A.; Moench, H.; Wersin, P.; Kugler, P.; Wenger, C. Solubility of antimony
613 and other elements in samples taken from shooting ranges. *J. Environ. Qual.* **2005,** *34* (1),
614 248-254.
615 (53) Zhao, X.; Liu, W.; Cai, Z.; Han, B.; Qian, T.; Zhao, D. An overview of preparation and
616 applications of stabilized zero-valent iron nanoparticles for soil and groundwater remediation.
617 *Water Res.* **2016,** *100*, 245-266.
618 (54) Gorman-Lewis, D.; Fein, J. B.; Burns, P. C.; Szymanowski, J. E.; Converse, J. Solubility
619 measurements of the uranyl oxide hydrate phases metaschoepite, compreignacite, Na–
620 compreignacite, becquerelite, and clarkeite. *J. Chem. Thermodyn.* **2008,** *40* (6), 980-990.

(55) Bots, P.; Morris, K.; Hibberd, R.; Law, G. T. W.; Mosselmans, J. F. W.; Brown, A. P.; Doutch, J.; Smith, A. J.; Shaw, S. Formation of stable uranium(VI) colloidal nanoparticles in conditions relevant to radioactive waste disposal. *Langmuir* **2014,** *30* (48), 14396-14405.

(56) Scheinost, A. C.; Kirsch, R.; Banerjee, D.; Fernandez-Martinez, A.; Zaenker, H.; Funke, H.; Charlet, L. X-ray absorption and photoelectron spectroscopy investigation of selenite reduction by Fe^{II}-bearing minerals. *J. Contam. Hydrol.* **2008,** *102* (3-4), 228-245.

(57) Scheinost, A. C.; Charlet, L. Selenite reduction by mackinawite, magnetite and siderite: XAS characterization of nanosized redox products. *Environ. Sci. Technol.* **2008,** *42* (6), 1984-1989.

(58) López de Arroyabe Loyo, R.; Nikitenko, S. I.; Scheinost, A. C.; Simonoff, M. Immobilization of selenite on Fe_3O_4 and Fe/Fe_3C ultrasmall particles. *Environ. Sci. Technol.* **2008,** *42* (7), 2451-2456.

(59) Mitsunobu, S.; Takahashi, Y.; Terada, Y. μ-XANES evidence for the reduction of Sb(V) to Sb(III) in soil from Sb mine tailing. *Environ. Sci. Technol.* **2010,** *44* (4), 1281-1287.

(60) Bès, R.; Rivenet, M.; Solari, P.-L.; Kvashnina, K. O.; Scheinost, A. C.; Martin, P. M. Use of HERFD–XANES at the U L_3- and M_4-edges to determine the uranium valence state on $[Ni(H_2O)_4]_3[U(OH,H_2O)(UO_2)_8O_{12}(OH)_3]$. *Inorg. Chem.* **2016,** *55* (9), 4260-4270.

(61) Kvashnina, K.; Butorin, S. M.; Martin, P.; Glatzel, P. Chemical state of complex uranium oxides. *Phys. Rev. Lett.* **2013,** *111* (25), 253002.

(62) Opel, K.; Weiss, S.; Hübener, S.; Zänker, H.; Bernhard, G. Study of the solubility of amorphous and crystalline uranium dioxide by combined spectroscopic methods. *Radiochim. Acta* **2007,** *95* (3), 143-149.

(63) Ma, B.; Fernandez-Martinez, A.; Grangeon, S.; Tournassat, C.; Findling, N.; Claret, F.; Koishi, A.; Marty, N. C. M.; Tisserand, D.; Bureau, S.; Salas-Colera, E.; Elkaïm, E.; Marini, C.; Charlet, L. Evidence of multiple sorption modes in layered double hydroxides using Mo ss structural probe. *Environ. Sci. Technol.* **2017,** *51* (10), 5531-5540.

(64) Sandberg, P. *Critical Evaluation of Factors Affecting Chloride Initiated Reinforcement Corrosion in Concrete*. Licentiate Thesis, University of Lund, Sweden, 1995.

(65) Kinniburgh, D.; Cooper, D. PhreePlot: Creating graphical output with PHREEQC. http://www.phreeplot.org.

(66) Rojo, H.; Scheinost, A. C.; Lothenbach, B.; Laube, A.; Wieland, E.; Tits, J. Retention of selenium by calcium aluminate hydrate (AFm) phases under strongly-reducing radioactive waste repository conditions. *Dalton Trans.* **2018,** *47* (12), 4209-4218.

(67) Langmuir, D. *Aqueous Environmental Geochemistry*; Prentice Hall, 1997.

(68) Burnol, A.; Garrido, F.; Baranger, P.; Joulian, C.; Dictor, M.-C.; Bodénan, F.; Morin, G.; Charlet, L. Decoupling of arsenic and iron release from ferrihydrite suspension under reducing conditions: A biogeochemical model. *Geochem. Trans.* **2007,** *8*, 12-12.

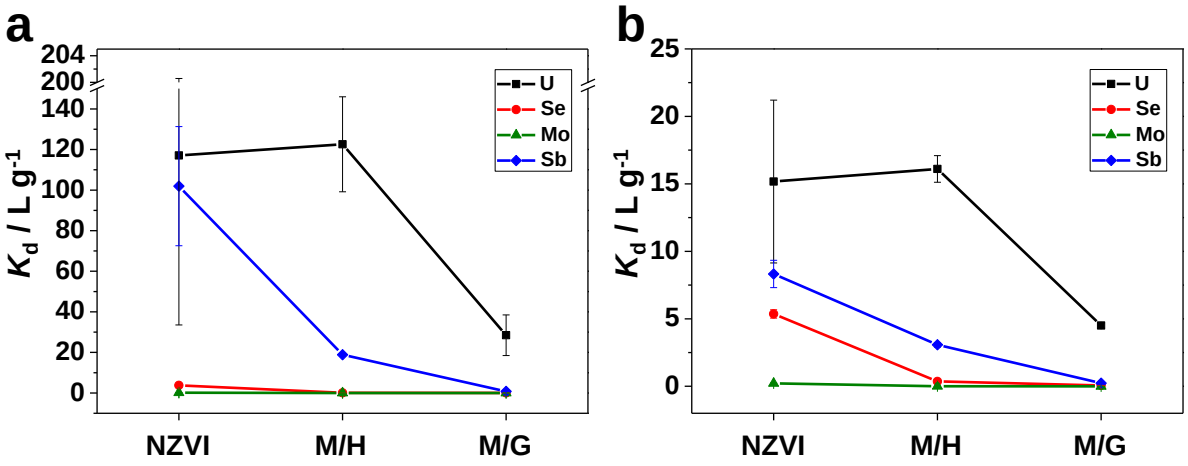

669

670 **Figure 1.** K_d values derived from batch sorption experiments, including the sorption of four
671 RN anions (i.e., U^{VI}, Se^{IV}, Mo^{VI}, and Sb^{V}) on NZVI, M/H, and M/G. (a) In N_2 atmosphere,
672 under continuous shaking, reacting 100 d. (b) Under 8.0 bar H_2 atmosphere, after 70 d reac-
673 tion time without shaking.

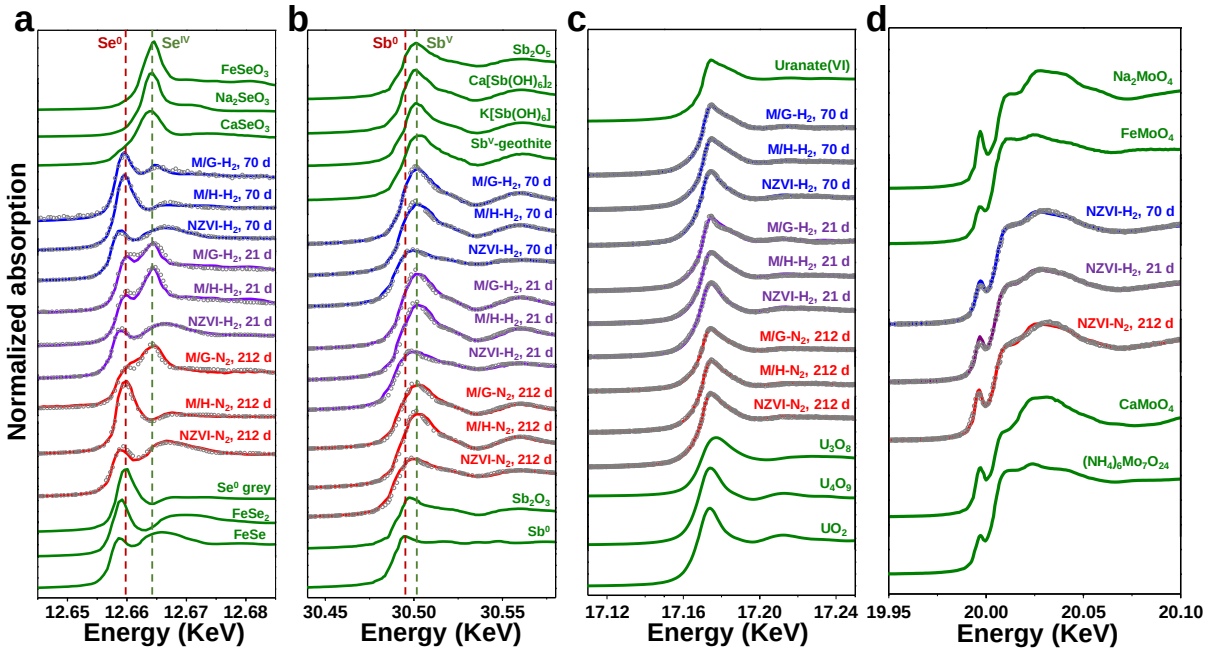

674

675 **Figure 2.** Experimental XANES spectra of reference compounds and RN analogues sorbed on
676 NZVI, M/H, and M/G in N_2 and H_2 atmosphere. (a) Se K-edge XANES spectra of selenium
677 sorption products. (b) Sb K-edge XANES spectra of antimony sorption products. (c) U L3-edge
678 XANES spectra of uranium sorption products. (d) Mo K-edge XANES spectra of molybdenum
679 sorption products. The grey dots represent the experimental data and the solid curves are the
680 LCF results.

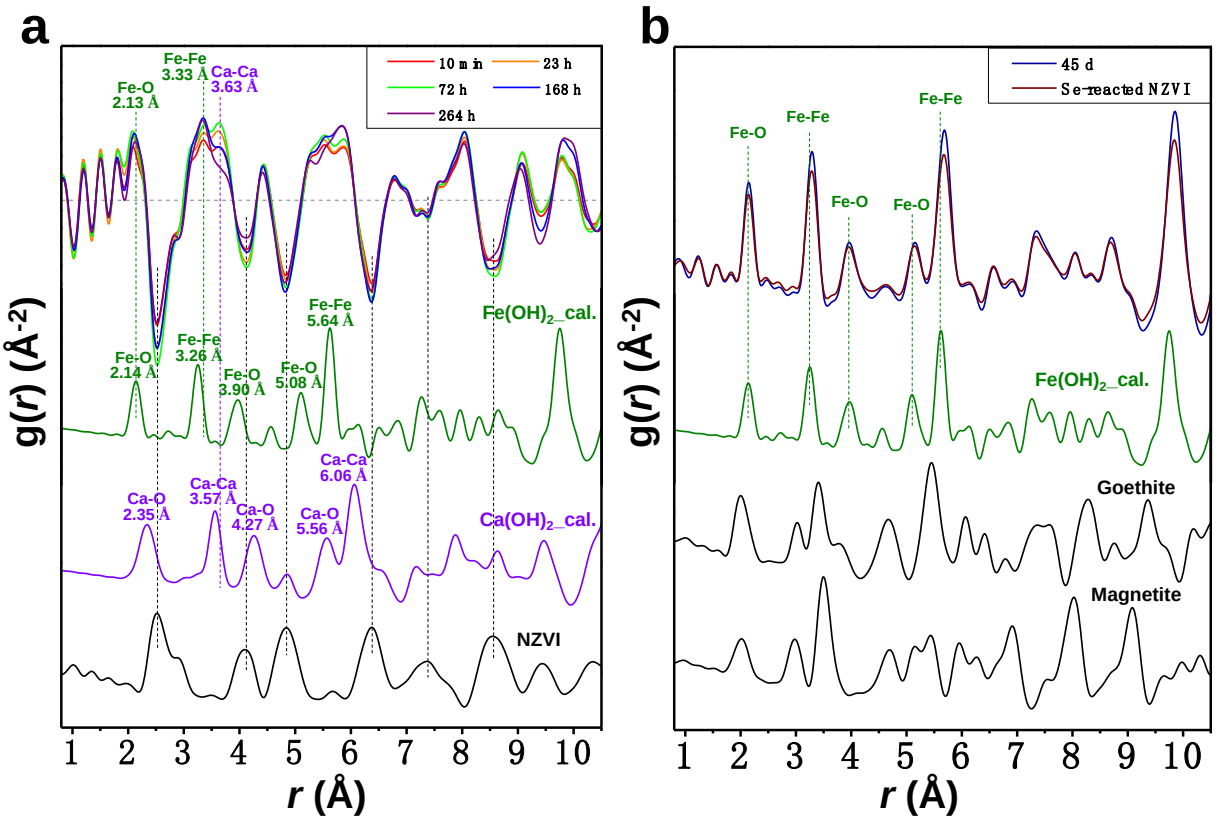

Figure 3. Differential PDF (d-PDF) and PDF patterns of reacted NZVI with CPW at different reaction time. (a) Experimental PDF of pristine NZVI and d-PDF of reacted NZVI; Calculated PDF references of $Fe(OH)_{2(cr)}$ and $Ca(OH)_2$. (b) PDF references are derived from calculated $Fe(OH)_{2(cr)}$, synthesized goethite and magnetite. Experimental PDF of reacted NZVI with CPW at 45 d and Se^{IV}-reacted NZVI is shown on the top.

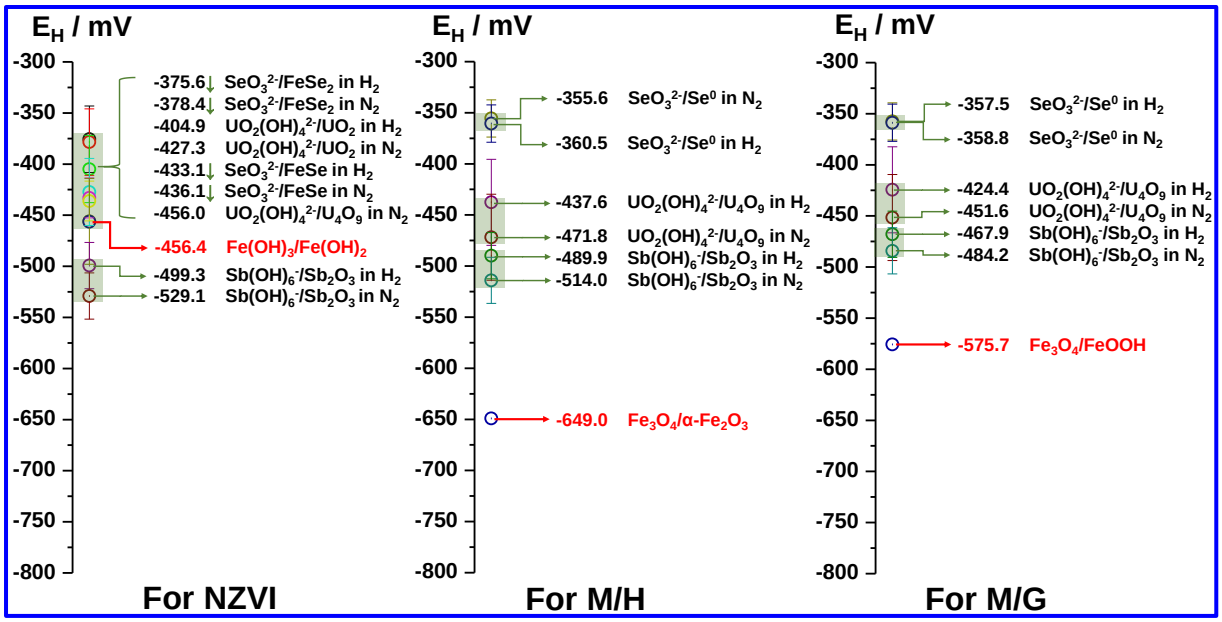

Figure 4. "In-situ" experimental Eh values for all the RNs systems and Eh values imposed by Fe-oxyhydroxides couples in stability domain of water. Down arrows put on SeO_3^{2-}/FeSe and SeO_3^{2-}/$FeSe_2$ indicates even lower Eh values due to possibly more diluted $Fe(OH)_4^-$.

Table 1. Quantification of RN analogue species (molar fraction) in N_2 reactors by LCF of XANES. Sorption products were equilibrated for ~212 d. Also reported is the concentration sum (Σ), which is not constrained to 100% for samples, and χ_v^2 value, both indicating good matches to the experimental spectra. Uncertainties are given by the number in brackets on the last digit(s), i.e., 77.6(1) represents 77.6 ± 0.1, and 53.1(1.2) represents 53.1 ± 1.2.

Se samples	FeSe (%)	$FeSe_2$ (%)	Se^0 (%)	$CaSeO_3$ (%)	Σ (%)	χ_v^2 × 10^{-3}
NZVI-N_2	77.6(2)	22.8(2)	-	-	100.4	0.9
M/H-N_2	-	-	100.0(2)	-	100.0	1.3
M/G-N_2	-	-	53.1(2.2)	53.4(2.1)	106.5	3.1

Sb samples	Sb^0 (%)	Sb_2O_3 (%)	$K[Sb(OH)_6]$ (%)	$Ca[Sb(OH)_6]_2$ (%)	Sb^V-Goe. (%)	Σ (%)	χ_v^2 × 10^{-3}
NZVI-N_2	68.5(15.2)	20.2(20.3)	11.7(20.4)	-	9.7(18.6)	110.2	1.8
M/H-N_2	-	14.0(4.5)	-	22.2(8.4)	75.4(8.7)	111.6	1.3
M/G-N_2	-	37.7(6.0)	-	19.3(11.9)	56.8(11.7)	113.9	2.4

U samples	UO_2 (%)	Uranate(VI) (%)	U_4O_9 (%)	Σ (%)	χ_v^2 × 10^{-3}
NZVI-N_2	13.2(9.1)	67.9(2.3)	19.5(11.0)	100.6	0.1
M/H-N_2	-	70.8(2.9)	29.8(13.7)	100.6	0.2
M/G-N_2	-	60.8(2.1)	39.4(1.9)	100.2	0.2

Mo samples	$FeMoO_4$ (%)	$CaMoO_4$ (%)	Na_2MoO_4 (%)	Σ (%)	χ_v^2 × 10^{-3}
NZVI-N_2	19.1(4.4)	44.1(6.1)	35.7(6.3)	99.0	0.4

724 **Table 2.** Half-cell reactions used for the computation of Eh values and the corresponding Eh^0
725 [a].

System	Half-cell reaction equation	Eh^0 / mV
Se(IV)/Se(0)	$SeO_3^{2-}{}_{(aq)} + 4e^- + 3H_2O \Leftrightarrow Se^0{}_{(s)} + 6OH^-$	-338.1
Se(IV)/Se(-I)	$2SeO_3^{2-}{}_{(aq)} + Fe(OH)_3^- + 10e^- + 6H_2O \Leftrightarrow FeSe_2 + 15OH^-$	-319.1
Se(IV)/Se(-II)	$SeO_3^{2-}{}_{(aq)} + Fe(OH)_3^- + 6e^- + 3H_2O \Leftrightarrow FeSe + 9OH^-$	-360.3
Sb(V)/Sb(III)	$2Sb(OH)_6^- + 4e^- \Leftrightarrow Sb_2O_3 + 6OH^- + 3H_2O$	-393.5
Sb(III)/Sb(0)	$Sb(OH)_4^- + 3e^- \Leftrightarrow Sb^0 + 4OH^-$	-641.3
U(VI)/U(IVS)	$4UO_2(OH)_4^{2-} + 6e^- \Leftrightarrow U_4O_{9(s)} + 14OH^- + H_2O$	-259.0
U(VI)/U(IV)	$UO_2(OH)_4^{2-} + 2e^- \Leftrightarrow UO_{2(s)} + 4OH^-$	-287.6
Fe(0)/$Fe(OH)_2$ couple	$Fe(OH)_2 + 2e^- \Leftrightarrow Fe^0 + 2OH^-$	-879.7
$Fe(OH)_2$/$Fe(OH)_3$ couple	$Fe(OH)_3 + e^- \Leftrightarrow Fe(OH)_2 + OH^-$	-486.4
M/H couple	$3Fe_2O_3 + 2e^- + H_2O \Leftrightarrow 2(Fe^{II}Fe^{III}{}_2)O_4 + 2OH^-$	-679.0
M/G couple	$6FeOOH + 2e^- \Leftrightarrow 2(Fe^{II}Fe^{III}{}_2)O_4 + 2OH^- + 2H_2O$	-605.6

726 [a] Experimental $[Fe]_{total}$ was under the ICP-OES detection limit (~10 ppb). Here, $Fe(OH)_3^-$
727 concentration is estimated at ~ 5 ppb (i.e., 10^{-7} M).
728

729

730 **Table of Contents (TOC)**

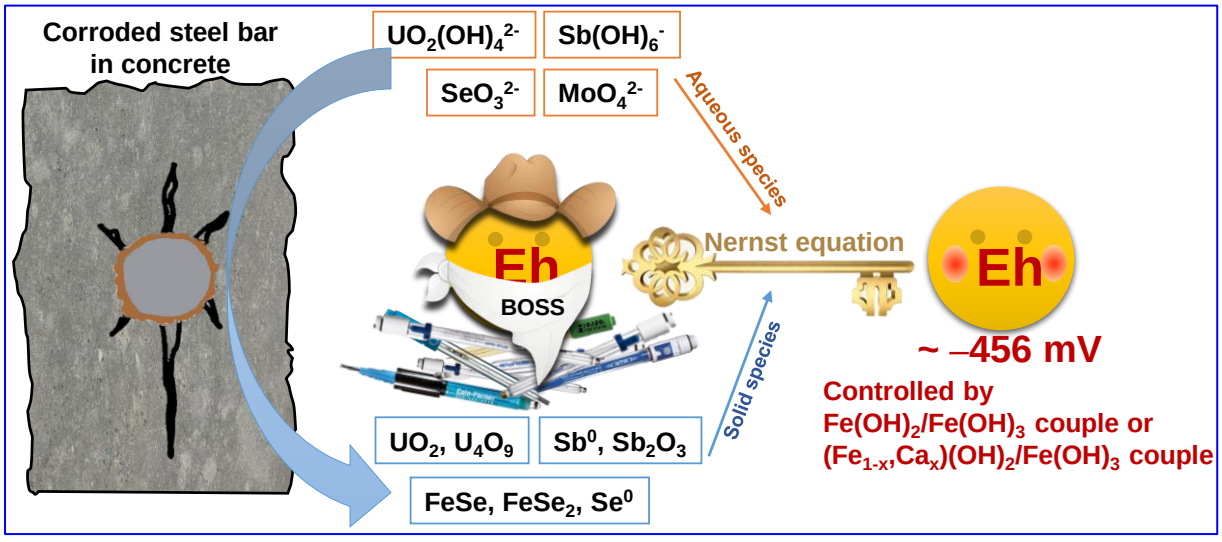

731